



OPEN

Enhanced optical and electrochemical properties of FeBTC MOF modified TiO₂ photoanode for DSSCs application

William Moloto¹, Pontsho Mbule², Edward Nxumalo^{1✉} & Bulelwa Ntsendwana^{3✉}

In this work, iron based 1, 3, 5-tricarboxylic acid (FeBTC) was prepared via microwave-assisted method and incorporated into TiO₂ via ultrasonic assisted method. The TiO₂-FeBTC nanocomposites were characterized by XRD, FTIR, Raman, BET, FESEM, HRTEM, TGA, UV-vis DRS and PL to understand their crystallographic, surface morphology, and optical characteristics. The Raman spectra showed a blue shift of E_g, A_{1g}, and B_{1g} peaks upon incorporation of FeBTC MOF onto TiO₂. HRTEM and XRD analysis confirmed a mixture of TiO₂ nanospheres and hexagonal FeBTC MOF morphologies with high crystallinity. The incorporation of FeBTC onto TiO₂ improved the surface area as confirmed by BET results, which resulted in improved absorption in the visible region as a results of reduced bandgap energy from 3.2 to 2.84 eV. The PL results showed a reduced intensity for TiO₂-FeBTC (6%) sample, indicating improved separation of electron hole pairs and reduced recombination rate. After fabrication of the TiO₂-FeBTC MOF photoanode, the charge transfer kinetics were enhanced at TiO₂-FeBTC MOF (6%) with Rp value of 966 Ω, as given by EIS studies. This led to high performance due to low charge resistance. Hence, high power conversion efficiency (PCE) value of 0.538% for TiO₂-FeBTC (6%) was achieved, in comparison with other loadings. This was attributed to a relatively high surface area which allowed more charge shuttling and thus better electrical response. Conversely, upon increasing the FeBTC MOF loading to 8%, significant reduction in efficiency (0.478%) was obtained, which was attributed to sluggish charge transfer and fast electron-hole pair recombination rate. The TiO₂-FeBTC (6%) may be a good candidate for use in DSSCs as a photoanode materials for improved efficiency.

Keywords TiO₂, TiO₂-FeBTC nanocomposites, Photoefficiency, DSSCs, Electrochemical impedance

Photovoltaics (PVs) are one of the important devices that enable the conversion of sunlight into energy. Photovoltaics can be categorised into three generations. The first generation is made of the crystalline and polycrystalline silicon solar cells, and are fabricated using very expensive materials and thus, difficult to acquire. The second generation utilizes copper indium gallium selenide (CIGS), cadmium telluride (CdTe), amorphous silicon (a-Si:H) and gallium arsenide (GaAs)^{1,2}. They are much cheaper compared to the first generation PVs, however, there has been toxicity concerns due to the use of transition elements². The third generation solar cells have emerged as promising alternatives due to their low cost of fabrication^{1,3,4}. In fact, research has suggested that they have the potential to replace conventional fossil fuels based on the materials use and affordable processes of fabrication⁵. Photovoltaics includes quantum dots, organic, perovskite and dye sensitized solar cells (DSSCs)^{2,6-8}. The third-generation solar cells are at a developmental stage and have shown promising potential. However, the efficiency of DSSCs is still low compared to other solar cells and more research has been devoted in improving their performance through utilisation of a wide range of cheaper materials and processes of fabrications^{3,5,9}. Noorasad et al. surveyed suitable methods of deposition for the preparation of flexible DSSCs⁹. This will allow the technology to be more affordable and accessible in many households. One of the most important components of DSSCs is the photoanode, since it is responsible for generation of the electrons upon light illumination³. Therefore, it is important to prioritise the development of photoanodes with optimal efficiencies for DSSCs applications. The

¹Institute for Nanotechnology and Water Sustainability, CSET, University of South Africa, Johannesburg 1710, South Africa. ²Department of Physics, CSET, University of South Africa, Johannesburg 1710, South Africa. ³Energy, Water, Environmental and Food Sustainable Technologies (EWEF-susTech), Johannesburg 1709, South Africa. ✉email: nxumaen@unisa.ac.za; bntsendwana@gmail.com

most commonly used photoanode material is TiO_2 , due to its attractive properties such as abundance, increased stability, non-toxicity, and the presence of mesopores in their structure^{10–12}. However, TiO_2 has several drawbacks, including large band gap energy, which limits its absorption capacity to UV region. This and low charge separation and charge transportation which further leads to fast recombination rates that eventually lead to a reduced photo-conversion efficiency.

The improvement of TiO_2 photoanode using other materials such as Al_2O_3 and carbon nanomaterials (graphene oxide, carbon nanotubes and carbon dots) is well documented in literature^{13–15}. For example, Choi et al. used Al_2O_3 to modify the surface of TiO_2 using solgel method¹⁶. It was found that uniform distribution on surface of TiO_2 increased the short circuit photocurrent and hence the overall energy conversion efficiency. The increase in light scattering upon addition of Al_2O_3 induced improved performance of DSSCs. Other researchers used reduced graphene oxide (rGO) to modify TiO_2 to improve the performance of DSSCs². The incorporation of rGO onto TiO_2 showed higher dye adsorption resulting in lower internal resistance and effect faster electron kinetics. The power conversion efficiency (PCE) value was improved to 6.69%, indicating almost 11% increase compared to the PCE of pure TiO_2 5.97%¹³. Carbon quantum dots (CQDs) with their quantum confinement have also been used to modify TiO_2 photoanodes⁴. The incorporation of CQDs improved the kinetics and light harvesting by suppressing bulk recombination rate of photogenerated electron–hole pairs. The photocurrent increased by 11.72 times compared to pure TiO_2 photoanode¹⁵.

On the other hand, metal organic frameworks (MOFs) have emerged as suitable materials that can be used as photoanode materials and sensitizers in DSSCs application due to their improved charge transportation and enhance light absorption (via organic linker engineering)¹⁷. Metal organic frameworks are coordinated compounds made up of organic ligands and polynuclear metal nodes that enable opening of a porous crystalline framework structure. Thus, they exhibit high specific surface area, up to $7000 \text{ m}^2/\text{g}^{-1}$ and they have been extensively used in various applications such as gas storage¹⁸, biomedical¹⁹, catalysis²⁰, gas–vapor separation²¹, energy and electronics²². In DSSCs applications, the high surface area materials such as MOFs are important as they allow more dyes to be adsorbed on the surface of the semiconductor material and therefore improve electron transportation, thereby hampering electron–hole recombination rates. Furthermore, MOFs exhibit suitable bandgap energy in the visible region, which satisfy the principle of photovoltaic device. It has been demonstrated that through metal–ligand charge transfer interaction, MOFs properties can be further enhanced via rational composition engineering^{17,23,24}. Hence, they have shown capabilities when either used directly as photoanode materials²⁵, or photosensitizers and electron shuttles to improve photoactivity and electron transportation²⁶. However, the catalytic activity of MOFs depends on the metal type used. Metal ions with *d* shell such as Nickel (Ni), Cu (Copper) and Cobalt (Co) are effective in tuning the bandgap energy^{27,28}. The iron-based MOFs have also showed better absorbing light properties in the visible region (380–800 nm). This aspect suggests that the iron-based MOFs can be used as photosensitizers²⁹. Additionally, they also exhibit good catalytic activity which can aid the charge transfer kinetics^{30,31}. Hence, in this study, we report the use of FeBTC MOF to modify the properties of TiO_2 for its potential use in DSSCs applications. The use of BTC (benzene-1, 3, 5-tricarboxylic acid) ligand is due its ease of dissolution which also requires no harmful solvent. Additionally, the ligands show good thermal stability, and this may allow the materials to be stable at higher temperatures. The incorporation of Fe-based MOFs in TiO_2 photoanodes is expected to improve the charge separation of electron hole pairs by retarding recombination rate.

Experimental procedure

Materials

Titanium isopropoxide ($\text{Ti}([\text{OCH}(\text{CH}_3)_2]_4$, 97%), trimesic acid (benzene-1,3,5-tricarboxylic acid) (H_3BTC , 95%), ethanol (96%), Isopropyl alcohol ($\text{C}_3\text{H}_8\text{O}$, 99.9%) polyethylene glycol (PEG 400) $\text{C}_2\text{nH}_4\text{n} + 2\text{O}_\text{n} + 1$, < 99%), ammonium hydroxide (NH_4OH , 25%), NaOH, 98%, iron chloride ($\text{FeCl}_3 \cdot 6\text{H}_2\text{O}$, 97%) were all purchased from Sigma-Aldrich (South Africa) and used without any further purification.

Synthesis of titanium dioxide (TiO_2)

The synthesis procedure for TiO_2 is described in our previous report¹². Typically, 15 mL of titanium isopropoxide and 45 mL of isopropyl alcohol were transferred into a 1000 mL beaker, where 250 mL of distilled water was used as hydrolysis catalyst. After adjusting the pH to 11.5 using NH_4OH , the mixture was stirred at 500 rpm at room temperature (27 °C) to create a homogenous solution. To catalyse the reaction, the solution mixture was heated for 20 h at 60 °C. The peptization process was followed by reduction in solution to about 30 mL to allow the white viscous suspension to be produced. The obtained white gel solution was washed 3 times using ethanol and then twice with distilled water. After air drying for 24 h, the material was further dried in the oven at 100 °C for 12 h. The TiO_2 powder was obtained by annealing for 2 h at 450 °C in a muffle furnace.

Synthesis of FeBTC MOF

The FeBTC MOF was synthesized via microwave assisted method. In a beaker containing 20 mL of polyethylene glycol (PEG-400), 40 mg of $\text{FeCl}_3 \cdot 6\text{H}_2\text{O}$ was added and allowed to stir for 15 min to create a suspension. In a 20 mL separate beaker, 4.2 mg of trimesic acid was added to 0.01 M sodium hydroxide (NaOH) solution. The two solutions were then mixed and transferred in a glass vial. The glass vial was then sealed with a Teflon lid and put in the microwave reaction vessel. The mixture was allowed to react for 30 min using maximum power of 500 W. After the reaction was complete, the vessel was allowed to cool to room temperature before the resultant suspension was washed with distilled water (3 times) and then with ethanol (2 times) using a centrifuge instrument. The powder was then dried in air for 48 h and thereafter dried for 12 h in an oven at 70 °C.

Synthesis of TiO₂-FeBTC nanocomposites

The synthesis of the nanocomposite materials was carried out using ultrasonic assisted method. Firstly, TiO₂ (1.5 g) powder was sonicated for 10 min in a beaker containing 10 mL of ethanol. In a separate beaker containing 10 mL of distilled water, FeBTC MOF (2 mg) was sonicated for 10 min. The two mixture were then transferred into a microwave reaction vessel for 30 min and allowed to cool to room temperature. The resulting suspension was washed in ethanol (3 times) and also in distilled water (2 times) using a centrifuge instrument. The powder was allowed to dry for 48 h in air and then dried in the oven for further 12 h at 70 °C. The powder was then sintered at 300 °C for 45 min. The TiO₂-FeBTC (2, 4, 6, and 8%) nanocomposites were obtained by varying the loadings of FeBTC MOF.

Characterization techniques

Various instrumental techniques were used to examine the properties of the as-synthesized materials. FTIR spectra PerkinElmer FTIR spectrometer Frontier (spectrum 100 spectrometer) using KBr pellet method at 4 cm⁻¹ resolution was used to study the presence of functional groups. A Witec Raman spectrometer (Alpha 300, TS 150) at 100× magnification and laser power source of 532 nm was used to collect Raman spectra. A Rigaku SmartLab X-ray diffractometer with Cu-Kα (λ = 0.154059 nm) radiation at 2°/min was used to perform XRD analysis. X-ray photoelectron spectroscopy (XPS) analysis was carried out using Thermo ESCalab 250 Xi spectrometer, with Al Kα (1486.7 eV) monochromatic X-ray radiation source which was calibrated by carbon deposit C (1 s) binding energy at 284.8 eV.

A JEOL JSM-7800F field emission scanning electron microscopy (FESEM) coupled with Oxford Aztec 350 X-Max80 electron dispersive spectroscopy (EDS), was used to record surface morphology and elemental analysis. High resolution TEM Tecnai G2F20 X-Twin MAT (Eindhoven, Netherlands) operating at 200 kV was used to analyse the internal morphology of the materials. Brunauer-Emmett-Teller (BET) nitrogen adsorption-desorption (Micromeritics Tristar Surface area and Porosity Analyser) was used to obtain the surface area, pore size and volume. To study the thermal stability of the materials under the inert environment from 35 to 900 °C at 10.00 °C/min heating rate a Perkin Elmer Pyris 1 Thermogravimetric analyser (TGA) was used. The optical properties were evaluated using PerkinElmer UV/Vis/NIR spectrometer Lambda 1050 from 200 to 800 nm wavelength range. A Horiba Fluorolog-3 Jobnyvon at the excitation wavelength of 325 nm was used to record photoluminescence spectra.

Fabrication of the photoanodes

Firstly, the FTO glass substrates (13.7 Ω) were soaked in a beaker containing soap and ultrasonicated for 15 min and rinsed with distilled water. They were further ultrasonicated in absolute ethanol for 15 min and rinsed with distilled water. The substrate was then baked in the furnace at 500 °C to remove any organic residues and thereafter stored in a clean desiccator to prevent any further contamination. The paste was obtained by dissolving 2 g of powder in 1.5 mL of dimethyl sulfoxide (DMSO) and allowed to sonicate for 10 min. The resultant paste was dropped on a clean FTO substrate and spin coated at 6000 rpm for 80 s. The coated films were then heated on the stove for 30 min at 90 °C, after which the films were baked in the furnace at 450 °C for 30 min (Fig. 1).

Photoelectrochemical studies

A computer-controlled potentiostat/galvanostat (galvanostat (Autolab, PGSTAT 302 N model, Metrohm, Swiss instruments) was used to obtain electrochemical data for the photoelectrodes. A three-set-up electrode, platinum foil, Ag/AgCl and prepared photoanodes (1.4 × 1.4 cm) were used as counter, reference and working electrodes respectively. An electrolyte containing 5 mM acetonitrile solution, 0.055 M LiI, 9 mM I₂ and 0.85 M LiClO₄ was used to carry the measurements. All EIS measurements were carried out at the frequency range of 1–100 kHz with voltage amplitude of 25 mV under the dark. To obtain photodensity measurements, a solar simulator equipped with a Xenon lamp and AM 1.5 filter under one-sun illumination (100 mW/cm²) was used.

Results and discussion

XRD analysis

To evaluate the crystallographic information, XRD analysis of as-synthesized samples was performed as presented in Fig. 2. The results showed that, TiO₂ exhibits indexed diffraction peaks of a tetragonal anatase phase (peaks at 2θ = 25.58° (101), 37.8.17° (004), 48.4° (200), 55.33° (105), 61.20° (204), 68.5° (220) and 76.1° (301) corresponding to the standard data, card no. 01-075-2552. These peaks were also observed in TiO₂-FeBTC (2, 4, 6 and 8%) nanocomposite materials. However, there was a red shift with reduced peak intensity in all of the nanocomposite materials, which highlights the interaction between TiO₂ and FeBTC. As it is reported elsewhere, the shifting of the peaks is related to structural relaxation upon the introduction of Fe-MOF on to TiO₂ and this is due to changes in lattice parameters^{12,32}.

The crystallite size, micro-strain and the D spacing results are given in Table 1. The crystallite size and micro-strain were estimated using the Eqs. (1) and (2) respectively:

$$D = \frac{0.9\lambda}{\beta \cos\theta}$$

$$\varepsilon = \frac{\beta}{4\tan\theta}$$

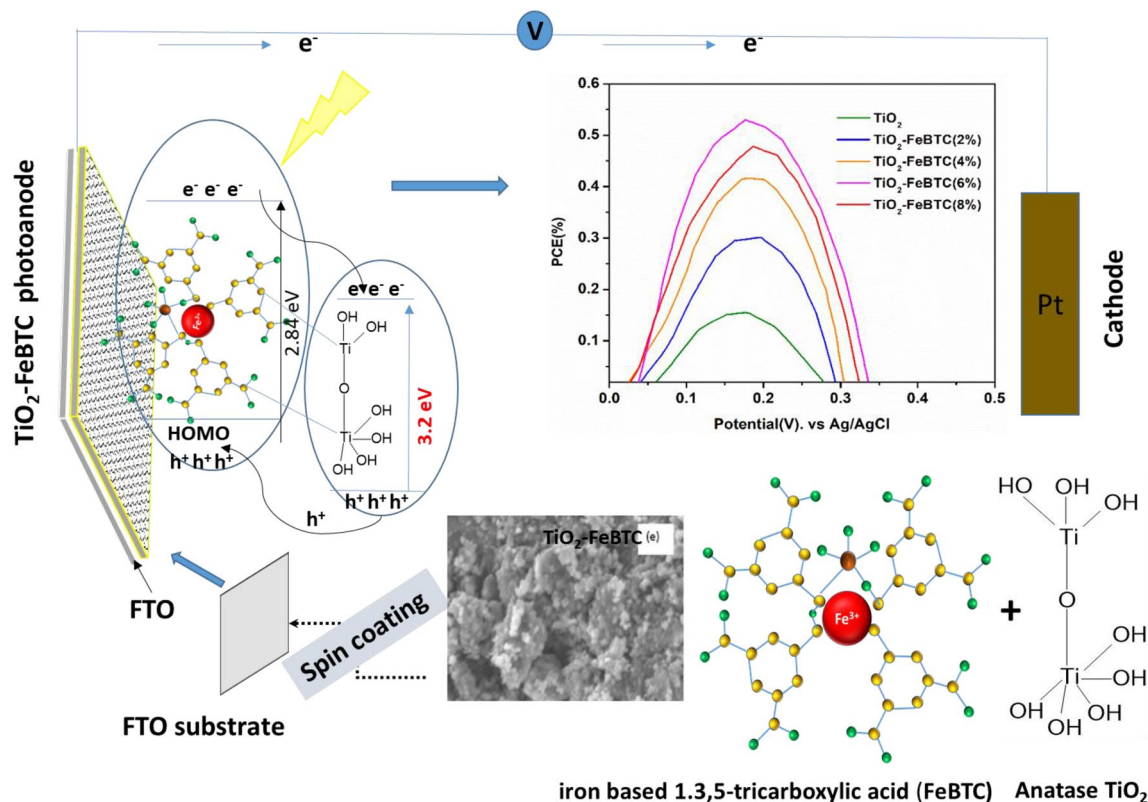


Figure 1. Schematic of the fabrication of TiO_2 -FeBTC photoelectrode.

where θ is the glancing Bragg's angle with the sample holder, $\lambda = 0.15418$ is the wavelength of $\text{CuK}\alpha$ radiation, and β is the line broadening at half the maximum intensity (FWHM). Accordingly, crystallite size ranged between 9.7–16 nm for the as-synthesized materials. There was a decrease in crystallite size and micro strain with FeBTC loading suggesting a change in crystallinity of TiO_2 upon the addition of FeBTC MOF.

To validate the chemical composition and oxidation state of the elements, XPS analysis was carried out as shown in Fig. 2b–d. The wide spectra in Fig. 2b showed the elemental constituents of pure TiO_2 and TiO_2 -FeBTC (6%) material. In Fig. 2c the high resolution spectra of TiO_2 showed the presence of two peaks at 463.8 and 458.1 eV, representing the $\text{Ti } 2p_{1/2}$ and $\text{Ti } 2p_{3/2}$ of the core level of Ti^{4+} , respectively. In TiO_2 -FeBTC (6%), these peaks are located at 464.1 and 458.3 eV for $\text{Ti } 2p_{1/2}$ and $\text{Ti } 2p_{3/2}$. Additionally, the Fe 2p spectra in Fig. 2d showed two main peaks at 724 and 732 eV which are assigned to $\text{Fe } 2p_{3/2}$ and $\text{Fe } 2p_{1/2}$ in Fe-BTC MOF, respectively. These two peaks with the presence of satellite peak at 729 eV suggest that the Fe-BTC MOF exist in the trivalent (Fe(III)) state. The O1s spectra in TiO_2 -FeBTC (6%), demonstrated a slight shift in binding energy, indicating a formation of C-Ti-O bonding (Fig. S1). The shift in binding energy suggest a strong interaction between the FeBTC and TiO_2 , which might facilitate the electron transfer between the material upon light illumination and applied potential/current density.

Morphological properties

SEM analyses of nanocomposite materials

SEM images of the as-synthesized materials are shown in Fig. 3. The SEM image of TiO_2 in Fig. 3a shows small aggregated spheres of nanoparticles. The aggregation may be due to stirring during the gelation in the synthesis step. The FeBTC MOF in Fig. 3b is characterized by irregular particles of different shape and size. The SEM images of TiO_2 -FeBTC MOF nanocomposites (Fig. 3c–f) are characterized by TiO_2 nanoparticles dispersed on the surface of larger FeBTC MOF nanoparticles. An increase in aggregation of nanoparticles, with an increase in FeBTC MOF loading was observed. The increase in aggregation may reduce the surface area of the materials and therefore hinder electron-charge transfer as there will be limited surface area for electron transfer reactions. Furthermore, EDS spectra in Fig. 3g showed the expected elements of TiO_2 (Ti, O, and C) and Fe-BTC (Fe, C, and O) in the nanocomposites. The EDS of TiO_2 -FeBTC (2, 4, 6, and 8%) are characterized by dominant Ti, O and C elements. Fe element was not observed in the nanocomposites materials and this could be due to low concentration used during the synthesis step.

HRTEM analysis

The morphology of the as-synthesized materials was further evaluated by HRTEM. Image J software was used to estimate the particle size of the materials. Figure 4a shows HRTEM image of TiO_2 which is characterized by aggregated nano-spheres with varying particle sizes, ranging between 4–35 nm. The variation of size was induced

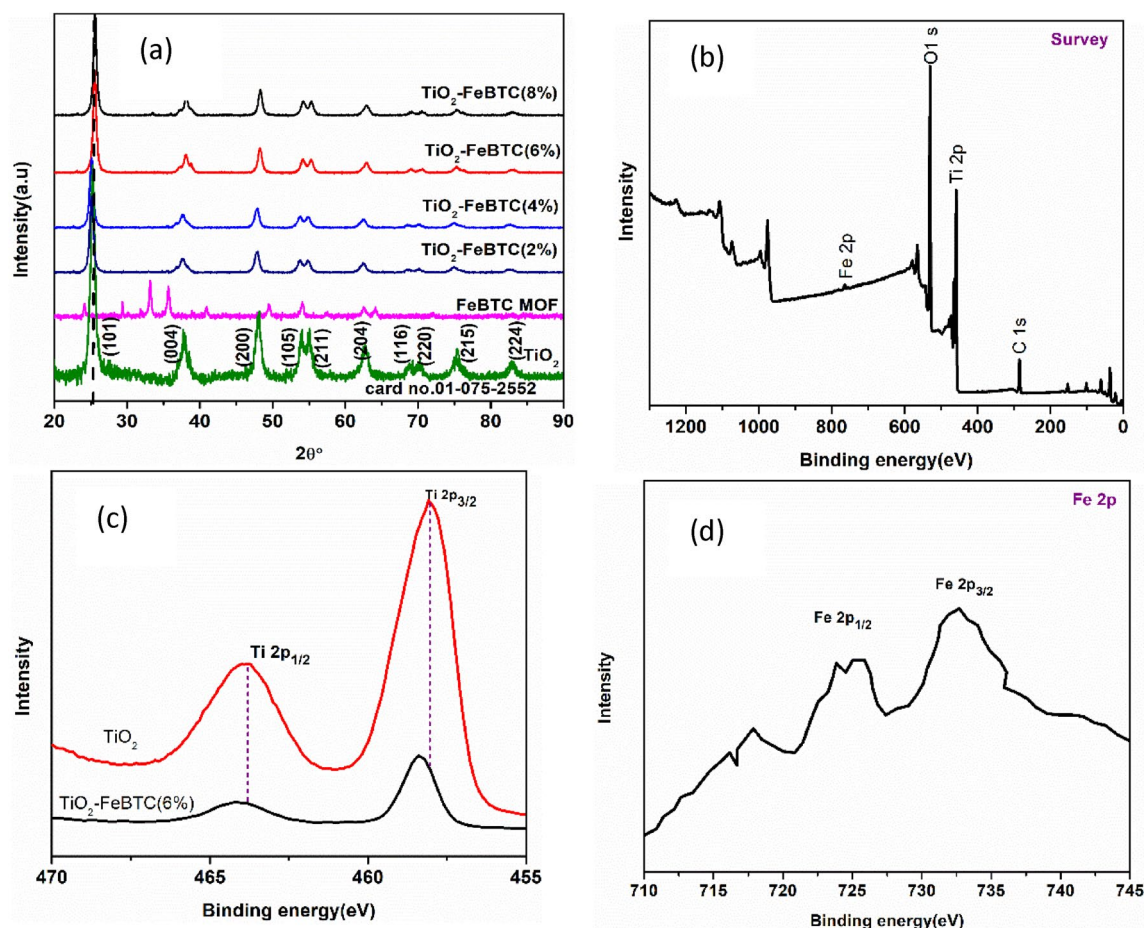


Figure 2. (a) XRD spectra of the as-synthesised materials (TiO_2 , FeBTC MOF and TiO_2 -FeBTC (2,4,6 and 8%) and XPS spectra: (b)) Wide spectra, (c) Ti 2p, and (d) Fe 2p.

Sample	Crystalline size	Micro-strain	D-spacing
TiO_2	16.40	0.211	0.332
FeBTC MOF	9.70	0.091	0.387
TiO_2 -FeBTC (2%)	15.10	0.204	0.344
TiO_2 -FeBTC (4%)	14.65	0.196	0.346
TiO_2 -FeBTC (6%)	12.81	0.197	0.359
TiO_2 -FeBTC (8%)	11.94	0.194	0.343

Table 1. Crystallite size, micro-strain and D-spacing of the as-synthesized materials.

by the stirring during the gelation process¹². The FeBTC MOF exhibited hexagonal shapes with poorly formed aggregated nanoparticles of different sizes as seen in Fig. 4b. The nanoparticles have a characteristic of moderate sorting which implies that the particle size variation is small. The particle size of FeBTC MOF ranged between 20–80 nm. The HRTEM images for TiO_2 -FeBTC(2,4,6 and 8%) nanocomposites are shown in Fig. 4c–f respectively. The HRTEM images of the nanocomposites are characterized by a mixture of smaller TiO_2 nanoparticles and much larger FeBTC MOF particles, attached to surface of each other. The FeBTC MOF nanoparticles are well dispersed on the surface of TiO_2 and this can be seen in all nanocomposites. The increase in loading of FeBTC MOF is also evident as the number of larger particles are observed at higher loadings from Fig. 4c–f. Hence, the aggregation of particles is more prevalent in TiO_2 -FeBTC (8%) nanocomposite (Fig. 4f) and thus, leading to a reduced pore sizes. The reduction of pore volume and sizes is an undesired consequence as it can reduce the charge transportation of electrons and also impact electron collection by the photoanode half of DSSCs, which will result in higher recombination rate of electron–hole pairs.

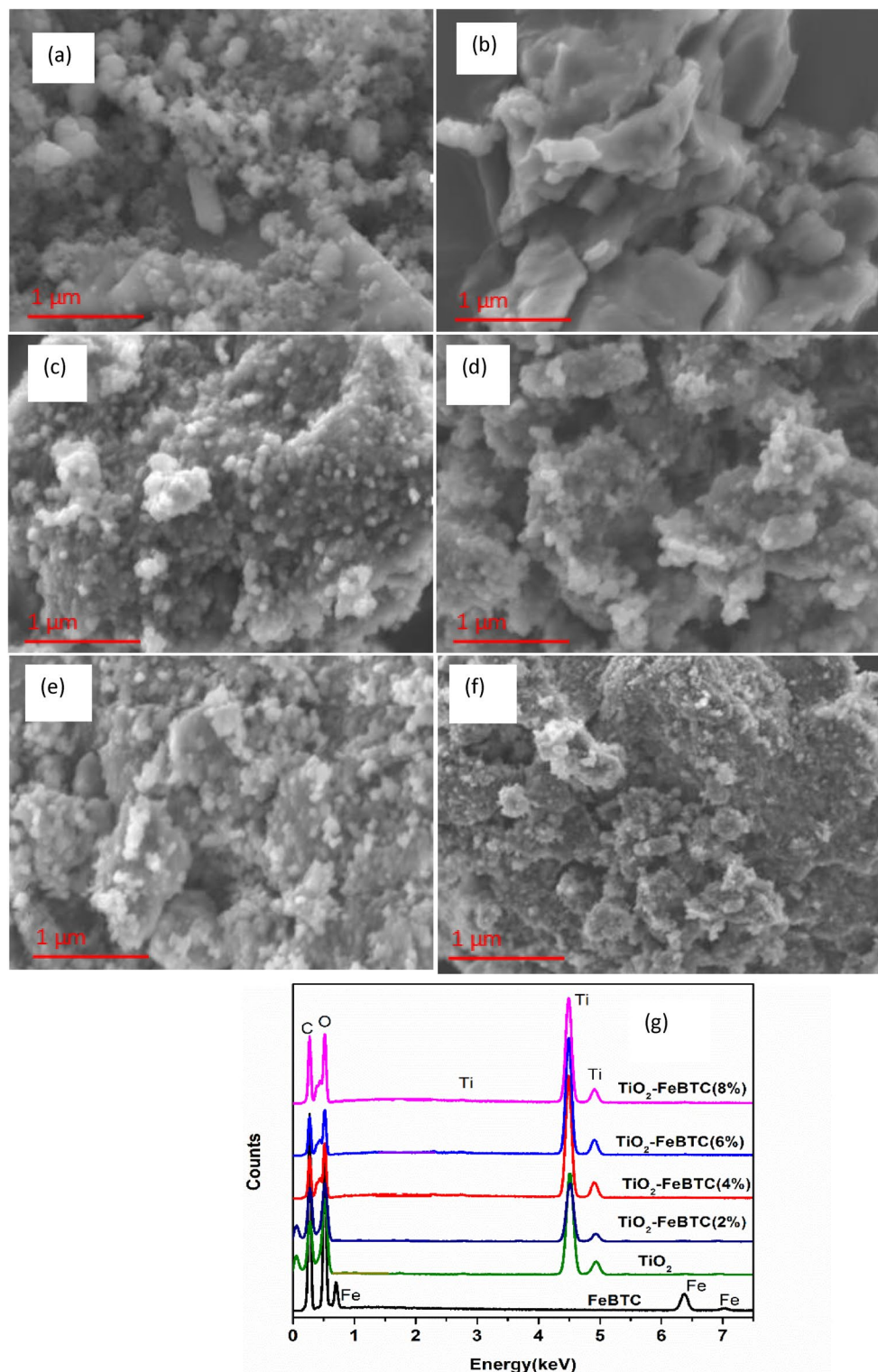


Figure 3. HRSEM images of (a) TiO_2 nanoparticles, (b) Fe-BTC MOF, (c–f) TiO_2 -Fe-BTC (2, 4, 6% and 8%) and (g) corresponding EDS spectra.

N₂ adsorption–desorption isotherms

The BET results in Table 2 show that TiO_2 exhibited a low specific surface area of $106.75 \text{ m}^2/\text{g}$, which is consistent with our previous findings¹². However, upon incorporation of FeBTC MOF, the surface area of $636.53 \text{ m}^2/\text{g}$, which was four times higher than that of TiO_2 was obtained. This means that, incorporation of MOF on TiO_2 matrix, considerably improves the specific surface areas. Consequently, the surface area was further improved with an increase of MOF loading by 2, 4, 6 and 8% reaching $188.5 \text{ m}^2/\text{g}$, $256.71 \text{ m}^2/\text{g}$, $328.54 \text{ m}^2/\text{g}$, and $336.21 \text{ m}^2/\text{g}$

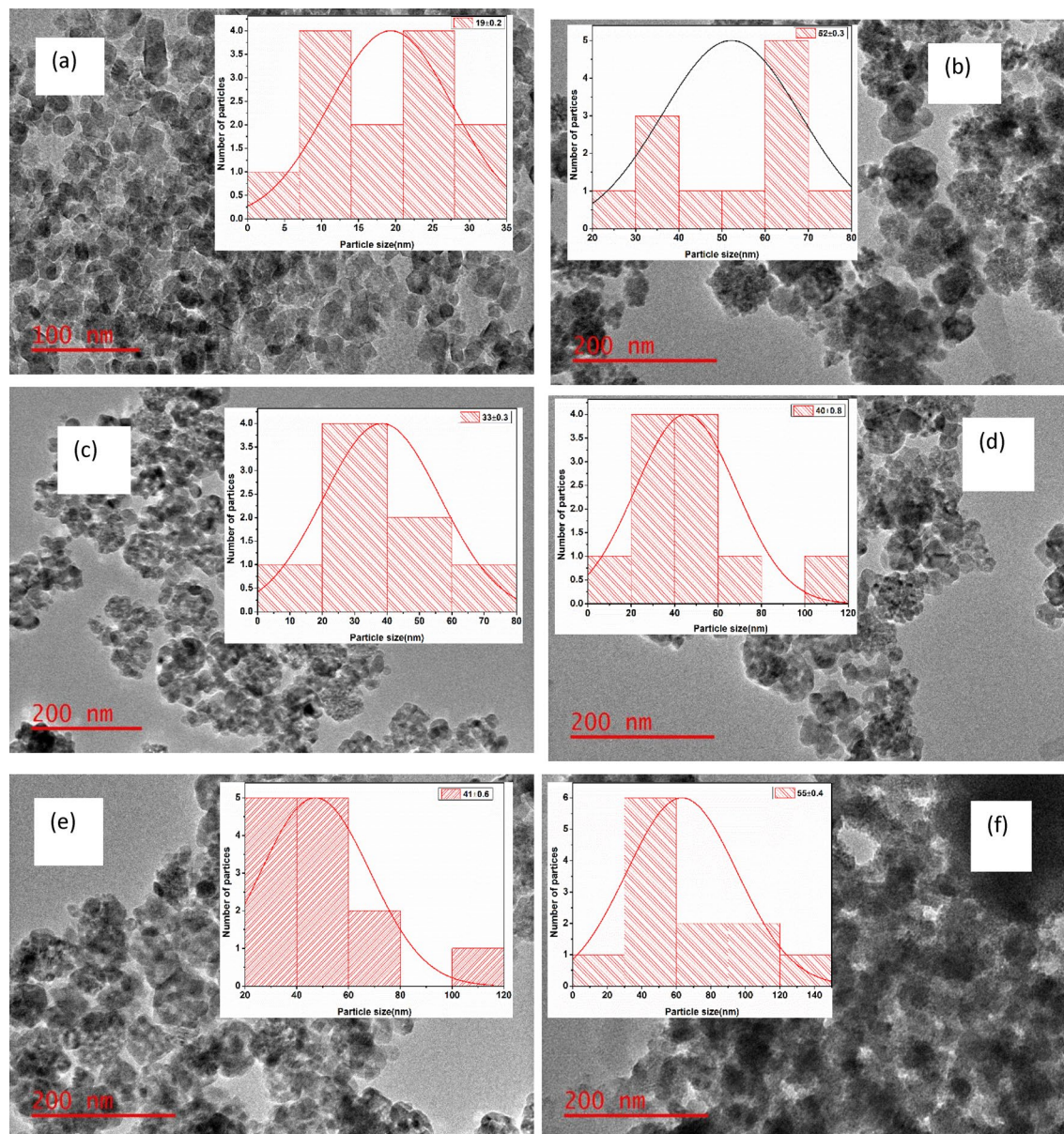


Figure 4. HRTEM images and particle size histograms of (a) TiO_2 , (b) FeBTC MOF, and (c) TiO_2 -FeBTC (2%), (d) TiO_2 -FeBTC (4%), (e) TiO_2 -FeBTC (6%) and (f) TiO_2 -FeBTC (8%).

Sample	Band gap (eV)	BET surface area (m^2/g)	Pore size (nm)	Pore volume (cm^3)	Particle size (nm)
TiO_2	3.21	106.75	3.5	0.36	19
FeBTC MOF	1.92	636.53	9.21	0.64	52
TiO_2 -FeBTC (2%)	2.91	188.50	3.7	0.35	33
TiO_2 -FeBTC (4%)	2.88	256.71	4.45	0.38	40
TiO_2 -FeBTC (6%)	2.85	328.54	7.2	0.44	41
TiO_2 -FeBTC (8%)	2.84	336.21	6.4	0.39	55

Table 2. Band gap energy, BET surface area, pore size, pore volume and particle size of as-synthesized materials.

respectively (Table 2). Similarly, the pore size and pore volume of the TiO₂-FeBTC nanocomposites also increased with an increase in MOF loading from 2 to 6%. However, the TiO₂-FeBTC (8%) nanocomposite showed a decrease in pore volume and pore size, which is attributed to higher aggregation of the Fe-BTC MOF and TiO₂ nanoparticles blocking the pores as evident from the SEM and HRTEM results.

Generally, DSSCs rely on the photoanode to absorb light and also generate electrons and therefore, the high surface area is an important property as it will aid in adsorption of the dye molecule on the surface of TiO₂-FeBTC MOF and thereby improving sunlight absorption. The N₂ adsorption-desorption isotherms corresponding to these samples are presented in Fig. 5a-f. The pure TiO₂ in Fig. 5b and the nanocomposite materials in Fig. 5c-f, showed a type IV isotherm which suggest that there are stronger lateral interactions between adsorbed molecules. The hysteresis loop showed by the nitrogen adsorption-desorption isotherm of TiO₂ confirms that

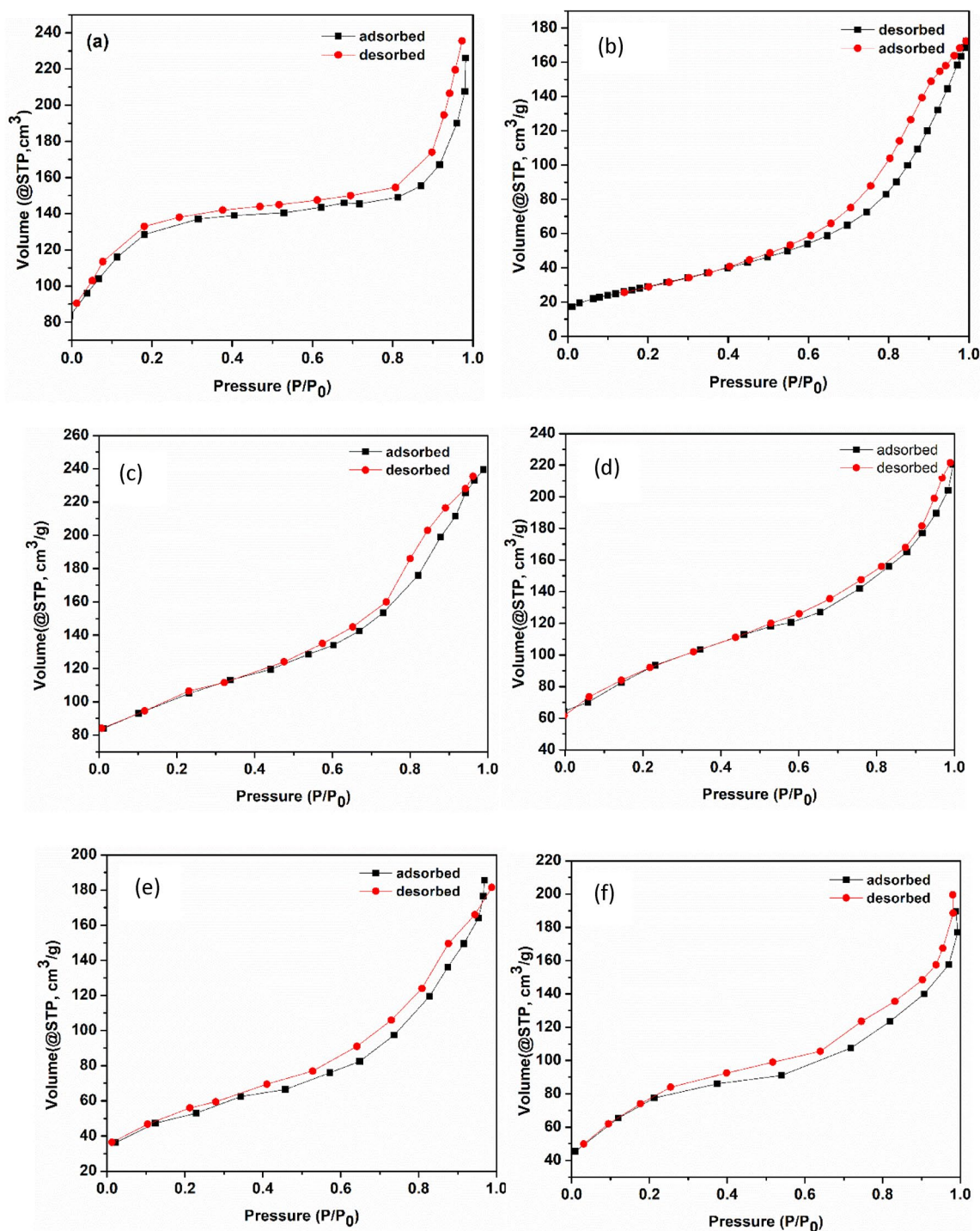


Figure 5. N₂ adsorption-desorption isotherms of (a) TiO₂, (b) FeBTC MOF, and (c) TiO₂-FeBTC (2%), (d) TiO₂-FeBTC (4%), (e) TiO₂-FeBTC (6%) and (f) TiO₂-FeBTC (8%).

the materials are mesoporous and resemble that of type H3 IUPAC (International Union of Pure and Applied Chemistry) classification. The FeBTC MOF isotherm in Fig. 5a, resembles that of type H1 which correlates with the porous material³³.

Functional and thermal properties

Raman analysis. The Raman spectra of pure TiO₂ and TiO₂-MOF nanocomposites (2, 4, 6 and 8%) is shown in Fig. 6a. The Raman spectrum of TiO₂, demonstrated distinct Raman active modes of the E_g (142.7 and 635.6 cm⁻¹), B_{1g} (396.5 cm⁻¹) and A_{1g} (514.1 cm⁻¹) which are characteristics of the anatase phase as also confirmed by XRD results. The Raman modes of anatase phase (E_g, B_{1g} and A_{1g}) are due to symmetric stretching vibration, symmetric bending vibration and the asymmetric bending vibration of O-Ti-O, respectively³⁴. The E_g peak of anatase at 142.7 cm⁻¹ decrease in intensity with an increase in Fe-BTC MOF loading, and there is blue-shift observed for all the E_g, B_{1g} and A_{1g} of Raman modes in the TiO₂-FeBTC (2, 4, 6 and 8%) nanocomposites. The increase in intensity is related to increase in crystallinity during the formation of the TiO₂-FeBTC nanocomposites due to three-dimensional phonon confinement³⁵. The shifting of Raman modes to lower wavenumber is related to an increase in crystal size of the TiO₂-FeBTC (2, 4, 6 and 8%) nanocomposite materials³⁶. In addition, the shifting in Raman peaks may be related to migration of electrons from the TiO₂ nanoparticles which decrease the band strength within the O-Ti-O bond^{12,37}. The change in Raman modes in all the nanocomposites spectra suggests that there is an interaction between the TiO₂ and FeBTC MOF.

Analysis of nano-hybrids by surface functional groups composition. The FTIR spectra of the TiO₂, Fe BTC MOF and TiO₂-FeBTC MOF (2, 4, 6, and 8%), are shown in Fig. 6b. The TiO₂ FTIR spectrum is characterized by bands observed between 3390 and 3560 cm⁻¹ associated with the O-H stretching and bending vibrations of the water molecules adsorbed on the surface. The peak at around 1635 cm⁻¹ is associated with the bending vibration of H-O-H group. The bending vibration of Ti-O-Ti in TiO₂ is assigned to the broad peak^{21,28} at 540–800 cm⁻¹. The spectrum of the FeBTC MOF is similar to the other reported by Delpiano et al. with the asymmetric stretching bands at 1629 and 1569 cm⁻¹. The bands at 1456 and 1390 cm⁻¹ were also observed which corresponds to the symmetric stretching of carboxylate groups in the BTC ligand³⁸. It was observed that the TiO₂-FeBTC MOF (2, 4, 6 and 8%) nanocomposite materials, demonstrated all characteristic bands which confirms the interaction

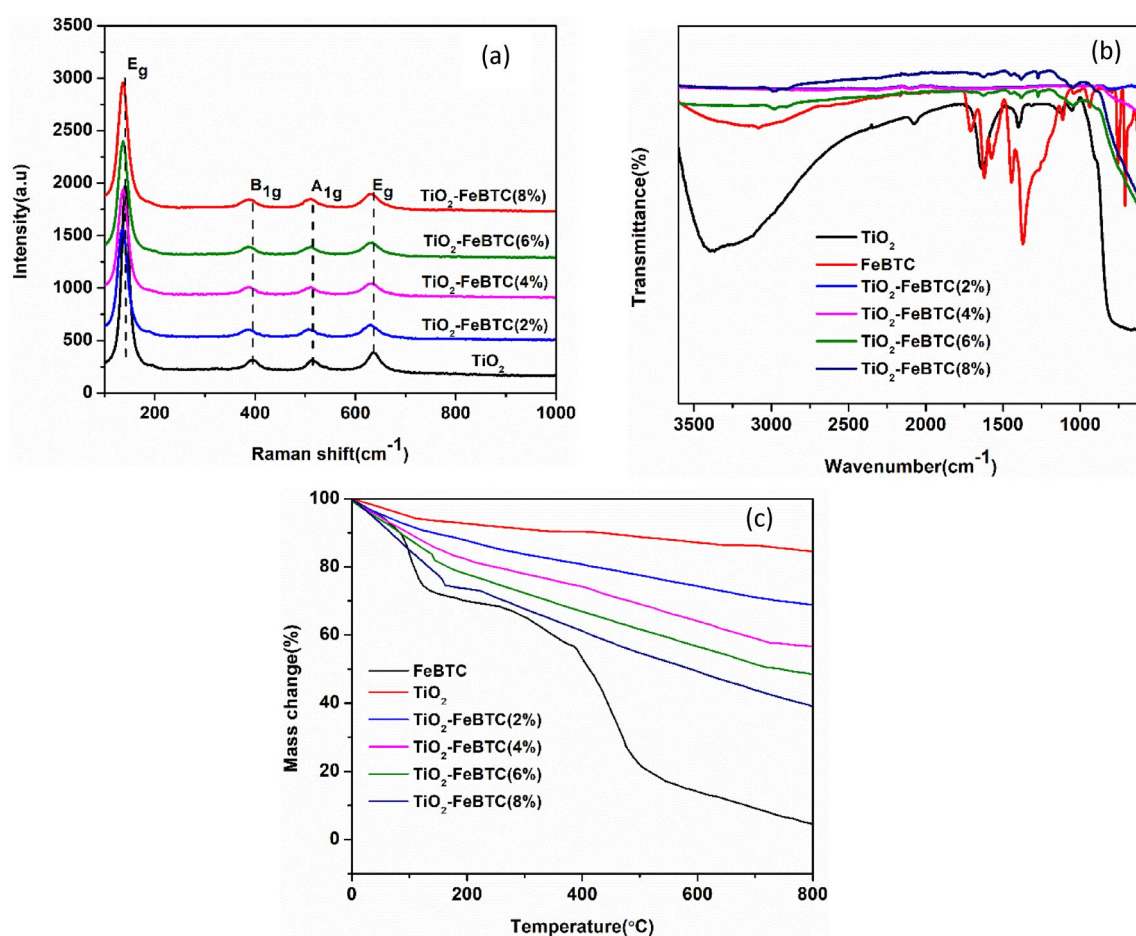


Figure 6. Shows the (a) FTIR, the (b) Raman spectra and (c) thermal gravimetric analysis of the as-synthesized materials.

of TiO₂ and FeBTC MOF materials. It is worth noting that there is a decrease in intensity in TiO₂-FeBTC (8%) nanocomposite due to increase in FeBTC concentration.

TGA analysis. To investigate the thermal stability of the as-synthesized materials, thermal gravimetric analysis (TGA) was performed as shown in Fig. 6c. The weight curve for Fe-BTC MOF shows several decomposition steps. At 100 °C, there is mass loss due to loss of moisture from water molecule. There is a mass loss due to destruction of the organic ligands was observed between 100 and 380 °C, while a total destruction of the Fe-BTC occurred from 400 to 550 °C, leaving only iron as the stable species. A minimal loss due to moisture below 100 °C was observed for TiO₂, however, it remains stable throughout the temperature. The TiO₂-FeBTC nanocomposites show relative stable curves compared to pure FeBTC MOF. However, as the Fe-BTC MOF loading is increased, the TiO₂ becomes less thermally stable as evident by TiO₂-FeBTC (2, 4, 6, and 8%) nanocomposites. This is induced by the less stable organic linker present in FeBTC MOF.

Optical and electrochemical properties

UV-Vis spectroscopic analysis

Figure 7a, shows the UV-Vis diffuse reflectance spectra of pure TiO₂, TiO₂-Fe-BTC MOF (2, 4, 6, and 8%) nanocomposite materials. The pure TiO₂ absorbs only in the UV region, with the absorption edge around 400 nm. The TiO₂-FeBTC nanocomposites spectra are characterized by two absorption peaks with different intensity at 422 nm and around 550 nm. The intensity of these peaks increases with an increase in FeBTC MOF loading, with the TiO₂-FeBTC (8%) showing the highest intensities. The appearance of the peak in the visible region suggest that there is an improvement in band gap energy which will allow TiO₂ to absorb in this region. The Tauc plots in Fig. 7b confirmed that as the FeBTC MOF loading is increased, the bandgap energy narrows, which allows efficient charge transfer of electro-hole pairs and hence reduce recombination rate. This was expected as the FeBTC MOF has an intense broad peak in the visible region of 400–620 nm. This is desirable in the fabrication of DSSCs because it allows photoanode to absorb more light and improve the electron shuttling in the conduction band of TiO₂, thereby improving the overall efficiency in the process.

Photoluminescence analysis

Photoluminescence (PL) was analysed to gain deeper insights into the photogenerated charge transport process in photocatalytic reaction by investigation of the efficiency of charge carrier trapping, transfer and migration and also understand the fate of electron-hole pairs in the as-synthesized nanocomposites. The recombination of the excited electrons and holes induce the PL emission. Under light irradiation, PL spectra was reported from excited electrons and holes, where the highest intensity correspond to higher recombination rate of electrons-hole pairs^{39,40}. The excitation wavelength was at 325 nm for all the as-synthesized materials under this study. In Fig. 8a, pristine TiO₂ has the higher intensity, which suggest that the material has the fastest recombination rate of holes and electrons relative to the FeBTC MOF and the nanocomposite materials. This indicate that the addition of FeBTC MOF reduced the recombination rate by bandgap engineering as suggested by UV-Vis studies. The addition of the MOF reduces the recombination rate of photogenerated charge carriers of electron-hole pairs. The 8% loading demonstrated a decrease in intensity which suggest an increase in recombination rate due to aggregation of FeBTC nanoparticles (Table 2). The increase in recombination rate may be related to the development of trapping sites which affects electron trapping in the shuttle process and therefore their development may greatly affect the performance of our materials in DSSCs.

EIS analyses for the TiO₂ and TiO₂-FeBTC MOF photoanodes

To further investigate the electron-hole pair separation behaviour of our materials, impedance studies were conducted on the prepared photoelectrodes. The photoanodes exhibited varied thickness of 17.26, 16.14, 14.11,

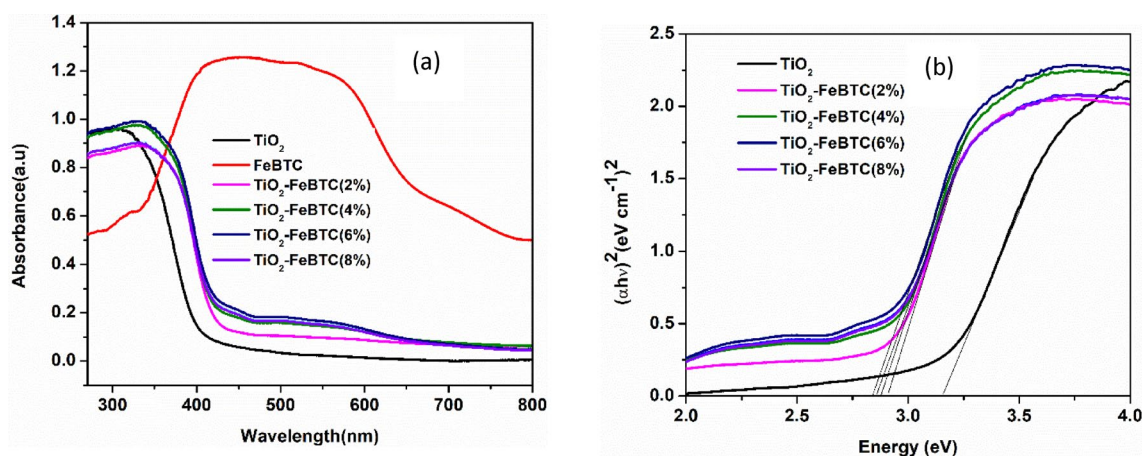


Figure 7. UV-Vis of TiO₂ and TiO₂-FeBTC MOF (2, 4, 6 and 8%) nano composites (a) and their corresponding Tauc plots (b).

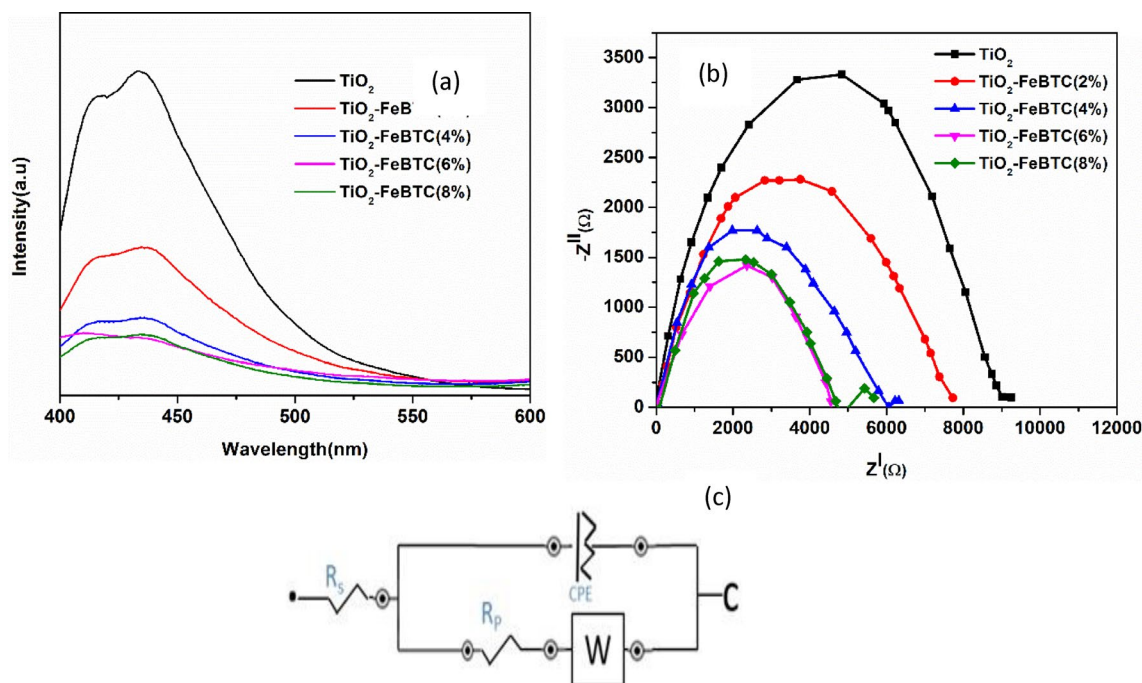


Figure 8. The EIS curves (a) and PL spectra (b) of the fabricated electrodes and (c) the Randles circuit used to fit EIS curves.

16.22 and 18.43 μm for TiO_2 , $\text{TiO}_2\text{-FeBTC}$ (2%), $\text{TiO}_2\text{-FeBTC}$ (4%), $\text{TiO}_2\text{-FeBTC}$ (6%) and $\text{TiO}_2\text{-FeBTC}$ (8%), respectively. EIS was conducted to investigate the charge transfer kinetics as shown with the Nyquist plots in Fig. 8b. The $\text{TiO}_2\text{-FeBTC}$ MOF nanocomposites were assessed, and the Nyquist plots are shown in Fig. 8b. The Randles circuit was used to fit the Nyquist curves and the equivalent circuit in Fig. 8c was used. Accordingly, the R_p values were 1572, 1351, 1174, 966 and 987 Ω for TiO_2 , $\text{TiO}_2\text{-FeBTC}$ (2, 4, 6 and 8%) nanocomposites. Based on the R_p values, there is a gradual decrease in charge resistance with an increase in Fe BTC MOF up to 6%. However, there is a sudden increase in charge transfer resistance when the loading is increased to 8%, which may be related to aggregation of $\text{TiO}_2\text{-FeBTC}$ nanoparticles, and thereby reducing the surface area and the pore size, which are the charge pathways and thus charge separation is compromised. This is supported by the SEM and BET results that showed that there is a decrease surface area due to increased aggregation. It was noted that the thickness of the photoanodes did not have correlation with the electron transportation. The decrease in charge transfer resistance with FeBTC MOF (6%) loading is due to the improved electron shuttling away from the hole in the TiO_2 surface and thus retarding recombination rate of electron-hole pairs.

Photoelectric performance of the $\text{TiO}_2\text{-FeBTC}$ MOF photoanodes

Photoelectric performance of the prepared thin film photoelectrodes are presented in Fig. 9a. Accordingly, under dark, the current was very low and therefore negligible. However, upon illumination, there was an increase in magnitude of current and again an increase in current with FeBTC MOF loading of the photoelectrode. The highest current was observed in the $\text{TiO}_2\text{-FeBTC}$ (6%) and was five times higher than that of pure TiO_2 . It is worth noting that beyond 8% loading of FeBTC MOF, there is a decrease in current generated. The charge resistance also starts to build up which inevitably increases the recombination rate. Power conversion efficiency as shown in Fig. 9b, was calculated from the I-V curves in Fig. 9a using the following equation:

$$\text{PCE}\% = \frac{J_p(E_{\text{rev}}^{\circ} - E_{\text{mea}} - E_{\text{cou}})}{I_0} \times 100\%$$

where, J_p is the photocurrent density (Am/cm^2), E_{rev}° is the standard state-reversible potential (1.43 vs Ag/AgCl) of the working electrode, E_{cou} is the open-circuit potential (vs Ag/AgCl) under the same working electrode experimental conditions, I_0 is the power density of the incident light and E_{mea} is the electrode potential of the working electrode whose photocurrent was tested under irradiation.

As expected from the I-V curves, the loading of FeBTC MOF increased the photoefficiency of the photoelectrodes. The photoefficiency values of TiO_2 , $\text{TiO}_2\text{-FeBTC}$ (2, 4, 6 and 8%) nanocomposites were found to be 0.145, 0.298, 0.421, 0.562, and 0.497%, respectively. The $\text{TiO}_2\text{-FeBTC}$ (6%) loading, exhibited high photo conversion efficiency. In comparison with pure TiO_2 photoanode, the photoefficiency of $\text{TiO}_2\text{-FeBTC}$ (6%) was over five times. These results are consistent with what we observed in the PL and EIS analysis. This suggest that $\text{TiO}_2\text{-FeBTC}$ (6%) can be a suitable candidate to use as a photoanode material in the development of DSSCs. To validate this work, the results were also compared to other reported TiO_2 photoelectrodes as shown in Table 3. The $\text{TiO}_2\text{-FeBTC}$ (6%) photoefficiency was comparable with other developed electrodes and therefore can be suitable for use in DSSCs.

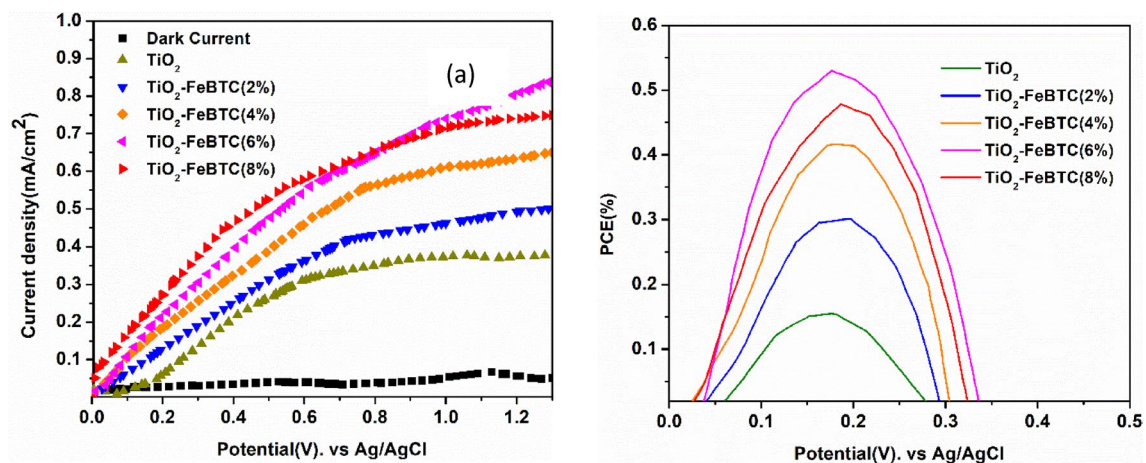


Figure 9. (a) I–V curves of TiO_2 (a) and TiO_2 -FeBTC (2, 4, 6 and 8%)/thin film photoelectrodes and (b) the corresponding photocurrent conversion efficiency. The experiment was performed in a solution with 5 mM acetonitrile solution, 0.055 M LiI, 9 mM I_2 and 0.85 M LiClO_4 in the dark and under illumination using one-sun illumination (100 mW/cm^2) and (b) shows the corresponding photo-conversion efficiency.

Photoanode	Method	R_p (Ω)	J (mA/cm^2)	PCE (%)	Bandgap	Refs.
TiO_2 -Fe-BTC (6%)	Ultrasonic assisted method	966	0.87	0.538	2.85	Current
ML(125)- NH_2/TiO_2 NRs	Hydrothermal	301	1.6	–	–	41
TiO_2 - WO_3 nanotube	Electrodeposition	–	0.85	0.52	3.0	42
TiO_2 -Graphene	Hydrothermal	–	1.4	–	2.6	43
TiO_2 -ZnBTC (2%)	Ultrasonic-assisted method	540	1.01	0.67	2.8	12
TiO_2/CdS	Electrodeposition	–	0.22	–	2.4	44
$\text{FeS}_2/\text{TiO}_2$	Wet chemistry	–	5.8	0.84	–	45
C@SiNWs/ TiO_2	Dip coating	23.9	5.56	1.17	–	46
Cd/ TiO_2	Hydrothermal	–	9.65	–	2.45	47

Table 3. The comparison of performance of other TiO_2 modified photoelectrodes with the TiO_2 -FeBTC (6%) photoelectrode.

Conclusions

This work reports the synthesis of TiO_2 -FeBTC nanocomposites through ultrasonic-assisted method and their subsequent fabrication into photoelectrode via spin coating technique. The surface, structural properties and optical properties were evaluated by XRD, FTIR, Raman, BET, TGA, FESEM, TEM, UV-Vis DRS, and PL techniques. Enhanced surface area and high pore volumes were observed after incorporation of FeBTC MOF onto TiO_2 , which also improved charge transfer kinetics and reduced electron-hole recombination rates as confirmed by EIS and PL, respectively. The TiO_2 -FeBTC (6%) showed good charge separation of electron-hole pairs due to low charge resistance. The improved charge transport due to surface area has allowed the 6% loading to have excellence photoelectrical response as confirmed by I–V curves. The I–V results have showed that there is a direct proportional relationship between the generated photocurrent and FeBTC MOF loading. The optimal photocurrent density was observed in the TiO_2 -FeBTC (6%) at 0.87 mA/cm^2 . This resulted in high PCE value of 0.538% of TiO_2 -FeBTC (6%). This was attributed of relatively high surface area, which allowed more charge shuttling and thus better electrical response. Further increase in loading above 6% resulted in higher aggregation of TiO_2 which gave rise to poor electron transport and thus higher recombination rate build-up. Therefore, it is necessary to optimise the loading of FeBTC MOF, as this can affect the performance of the photoanode in DSSCs. Based on the assessed performance of TiO_2 -FeBTC (6%), can form a viable candidate as a photoanode materials for DSSCs.

Data availability

The datasets used and/or analysed during the current study available from the corresponding author on reasonable request.

Received: 1 February 2022; Accepted: 14 April 2022

Published online: 17 May 2024

References

- Dambhare, M. V., Butey, B. & Moharil, S. V. Solar photovoltaic technology: A review of different types of solar cells and its future trends. *J. Phys. Conf. Ser.* <https://doi.org/10.1088/1742-6596/1913/1/012053> (2021).
- Ahmad, K. S., Naqvi, S. N. & Jaffri, S. B. Systematic review elucidating the generations and classifications of solar cells contributing towards environmental sustainability integration. *Rev. Inorg. Chem.* **41**, 21–39. <https://doi.org/10.1515/revic-2020-0009> (2021).
- Sharma, K., Sharma, V. & Sharma, S. S. Dye-sensitized solar cells: Fundamentals and current status. *Nanoscale Res. Lett.* **13**, 381–426. <https://doi.org/10.1186/s11671-018-2760-6> (2018).
- Shelke, R. S. Status and perspectives of dyes used in dye sensitized solar cells. *Int. J. Renew. Energy Resour.* **3**, 54–61 (2014).
- Devadiga, D., Selvakumar, M., Shetty, P. & Santosh, M. S. Recent progress in dye sensitized solar cell materials and photo-supercapacitors: A review. *J. Power Sources* **493**, 229698–229754. <https://doi.org/10.1016/j.jpowsour.2021.229698> (2021).
- Yan, J. & Saunders, B. R. Third-generation solar cells: A review and comparison of polymer: Fullerene, hybrid polymer and perovskite solar cells. *RSC Adv.* **4**, 43286–43314. <https://doi.org/10.1039/c4ra07064j> (2014).
- Buitrago, E., Novello, A. M. & Meyer, T. Third-generation solar cells: Toxicity and risk of exposure. *Helv. Chim. Acta* <https://doi.org/10.1002/hlca.202000074> (2020).
- Mirabi, E., Akrami Abarghuie, F. & Arazi, R. Integration of buildings with third-generation photovoltaic solar cells: A review. *Clean Energy* **5**, 505–526. <https://doi.org/10.1093/ce/zkab031> (2021).
- Rondán-Gómez, V. *et al.* Recent advances in dye-sensitized solar cells. *Appl. Phys. A Mater. Sci. Process.* **125**, 1–24. <https://doi.org/10.1007/s00339-019-3116-5> (2019).
- Noorasid, N. S. *et al.* Current advancement of flexible dye sensitized solar cell: A review. *Optik (Stuttg)* **254**, 168089. <https://doi.org/10.1016/j.ijleo.2021.168089> (2022).
- Castillo-robles, J. A., Rocha-rangel, E., Ram, A. & Caballero-Rico, F. C. Advances on dye-sensitized solar cells (DSSCs) nanostructures and natural colorants: A review. *J. Compos. Sci.* **11**, 288 (2021).
- Moloto, W., Mbule, P., Nxumalo, E. & Ntsendwana, B. Stabilizing effects of zinc(II)-benzene-1,3,5-tricarboxylate metal organic frameworks on the performance of TiO₂ photoanodes for use in dye-sensitized solar cells. *J. Photochem. Photobiol. A Chem.* **407**, 113063–113074. <https://doi.org/10.1016/j.jphotochem.2020.113063> (2021).
- Wei, L. *et al.* Reduced graphene oxide modified TiO₂ semiconductor materials for dye-sensitized solar cells. *RSC Adv.* **6**, 100866–100875. <https://doi.org/10.1039/c6ra22121b> (2016).
- Kilic, B. *et al.* Preparation of carbon nanotube/TiO₂ mesoporous hybrid photoanode with iron pyrite (FeS₂) thin films counter electrodes for dye-sensitized solar cell. *Sci. Rep.* **6**, 1–9. <https://doi.org/10.1038/srep27052> (2016).
- Zhou, T. *et al.* Carbon quantum dots modified anatase/rutile TiO₂ photoanode with dramatically enhanced photoelectrochemical performance. *Appl. Catal. B Environ.* **269**, 118776–118785. <https://doi.org/10.1016/j.apcatb.2020.118776> (2020).
- Choi, S. C., Lee, H. S., Oh, S. J. & Sohn, S. H. Light scattering TiO₂ particles surface-modified by Al₂O₃ coating in a dye-sensitized solar cell. *Phys. Scr.* **85**, 25801–25805. <https://doi.org/10.1088/0031-8949/85/02/025801> (2012).
- Spoerke, E. D. *et al.* MOF-sensitized solar cells enabled by a pillared porphyrin framework. *J. Phys. Chem.* **124**, 4816–4824. <https://doi.org/10.1021/acs.jpcc.6b11251> (2017).
- Li, H. *et al.* Porous metal-organic frameworks for gas storage and separation: Status and challenges. *EnergyChem* **1**, 100006–100044. <https://doi.org/10.1016/j.enchem.2019.100006> (2019).
- Yang, J. & Yang, Y. W. Metal-organic frameworks for biomedical applications. *Small* **16**, 1–24. <https://doi.org/10.1002/sml.201906846> (2020).
- Loera-Serna, S. & Ortiz, E. Catalytic applications of metal-organic frameworks. *Adv. Catal. Mater. Photocatal. Other Curr. Trends* <https://doi.org/10.5772/61865> (2016).
- Mohideen, M. I. H. *et al.* A fine-tuned MOF for gas and vapor separation: A multipurpose adsorbent for acid gas removal, dehydration, and BTX sieving. *Chem* **3**, 822–833. <https://doi.org/10.1016/j.chempr.2017.09.002> (2017).
- Wang, H., Zhu, Q. L., Zou, R. & Xu, Q. Metal-organic frameworks for energy applications. *Chem* **2**, 52–80. <https://doi.org/10.1016/j.chempr.2016.12.002> (2017).
- Hendon, C. H. *et al.* Engineering the optical response of the titanium-MIL-125 metal-organic framework through ligand functionalization. *J. Am. Chem. Soc.* **135**, 10942–10945. <https://doi.org/10.1021/ja405350u> (2013).
- Chueh, C. C. *et al.* Harnessing MOF materials in photovoltaic devices: Recent advances, challenges, and perspectives. *J. Mater. Chem. A* **7**, 17079–17095. <https://doi.org/10.1039/c9ta03595h> (2019).
- Lee, D. Y. *et al.* Enhanced photovoltaic performance of Cu-based metal-organic frameworks sensitized solar cell by addition of carbon nanotubes. *Sci. Rep.* **4**, 1–5. <https://doi.org/10.1038/srep03930> (2014).
- Cardoso, J. C. *et al.* MOFs based on ZIF-8 deposited on TiO₂ nanotubes increase the surface adsorption of CO₂ and its photoelectrocatalytic reduction to alcohols in aqueous media. *Appl. Catal. B Environ.* **225**, 563–573. <https://doi.org/10.1016/j.apcatb.2017.12.013> (2018).
- Rosi, N. L. *et al.* Rod packings and metal-organic frameworks constructed from rod-shaped secondary building units. *J. Am. Chem. Soc.* **127**, 1504–1518. <https://doi.org/10.1021/ja045123o> (2005).
- Tu, M. & Fischer, R. A. Heteroepitaxial growth of surface mounted metal-organic framework thin films with hybrid adsorption functionality. *J. Mater. Chem. A* **2**, 2018–2022. <https://doi.org/10.1039/c3ta13812g> (2014).
- Laurier, K. G. M. *et al.* Iron(III)-based metal-organic frameworks as visible light photocatalysts. *J. Am. Chem. Soc.* **135**, 14488–14491. <https://doi.org/10.1021/ja405086e> (2013).
- Lionet, Z. *et al.* Water oxidation reaction promoted by MIL-101(Fe) photoanode under visible light irradiation. *Res. Chem. Intermed.* **44**, 4755–4764. <https://doi.org/10.1007/s11164-018-3271-x> (2018).
- You, S. M. *et al.* Fe/Ni bimetallic organic framework deposited on TiO₂ nanotube array for enhancing higher and stable photoelectrochemical activity of oxygen evolution reaction. *Nanomaterials* **10**, 1–13. <https://doi.org/10.3390/nano10091688> (2020).
- Rajender, G. & Giri, P. K. Strain induced phase formation, microstructural evolution and bandgap narrowing in strained TiO₂ nanocrystals grown by ball milling. *J. Alloys Compd.* **676**, 591–600. <https://doi.org/10.1016/j.jallcom.2016.03.154> (2016).
- Allothman, Z. A. A review: Fundamental aspects of silicate mesoporous materials. *Materials (Basel)* **5**, 2874–2902. <https://doi.org/10.3390/ma5122874> (2012).
- Zhang, Y. *et al.* Asymmetric lattice vibrational characteristics of rutile TiO₂ as revealed by laser power dependent Raman spectroscopy. *J. Phys. Chem. C* **117**, 24015–24022 (2013).
- Swamy, V. *et al.* Size-dependent modifications of the Raman spectrum of rutile TiO₂. *Appl. Phys. Lett.* **89**, 163118. <https://doi.org/10.1063/1.2364123> (2006).
- Ekoi, E. J., Gowen, A., Dorrepaal, R. & Dowling, D. P. Results in physics characterisation of titanium oxide layers using Raman spectroscopy and optical profilometry: Influence of oxide properties. *Results Phys.* **12**, 1574–1585. <https://doi.org/10.1016/j.rinp.2019.01.054> (2019).
- Lian, P. *et al.* Large reversible capacity of high quality graphene sheets as an anode material for lithium-ion batteries. *Electrochim. Acta* **55**, 3909–3914. <https://doi.org/10.1016/j.electacta.2010.02.025> (2010).
- Delpiano, G. R. *et al.* Adsorption of malachite green and alizarin red dyes using Fe-BTC metal organic framework as adsorbent. *Int. J. Mol. Sci.* **22**, 1–16. <https://doi.org/10.3390/ijms22020788> (2021).

39. Mafa, P. J., Ntsendwana, B., Mamba, B. B. & Kuvarega, A. T. Visible light driven ZnMoO/BiFeWO/RGO Z-scheme photocatalyst for the degradation of anthraquinonic dye light photocatalyst for the degradation of anthraquinonic dye. *J. Phys. Chem. C* <https://doi.org/10.1021/acs.jpcc.9b05008> (2019).
40. Wang, X. *et al.* Novel BiOCl-C₃N₄ heterojunction photocatalysts: In situ preparation via an ionic-liquid-assisted solvent-thermal route and their visible-light photocatalytic activities. *Chem. Eng. J.* <https://doi.org/10.1016/j.cej.2013.08.112> (2013).
41. Yoon, J. W. *et al.* NH₂-MIL-125(Ti)/TiO₂ nanorod heterojunction photoanodes for efficient photoelectrochemical water splitting. *Appl. Catal. B Environ.* **244**, 511–518. <https://doi.org/10.1016/j.apcatb.2018.11.057> (2019).
42. Ali, H., Ismail, N., Amin, M. S. & Mekewi, M. Decoration of vertically aligned TiO₂ nanotube arrays with WO₃ particles for hydrogen fuel production. *Front. Energy* **12**, 249–258. <https://doi.org/10.1007/s11708-018-0547-1> (2018).
43. Ahmed, N., Farghali, A. A., El Roubi, W. M. A. & Allam, N. K. Enhanced photoelectrochemical water splitting characteristics of TiO₂ hollow porous spheres by embedding graphene as an electron transfer channel. *Int. J. Hydrog. Energy* **42**, 29131–29139. <https://doi.org/10.1016/j.ijhydene.2017.10.014> (2017).
44. Chi, Y. J. *et al.* Preparation and photoelectric performance of ITO/TiO₂/CdS composite thin films. *J. Photochem. Photobiol. A Chem.* **195**, 357–363. <https://doi.org/10.1016/j.jphotochem.2007.11.002> (2008).
45. Wang, D. Y. *et al.* Iron pyrite/titanium dioxide photoanode for extended near infrared light harvesting in a photoelectrochemical cell. *Sci. Rep.* **6**, 1–7. <https://doi.org/10.1038/srep20397> (2016).
46. Devarapalli, R. R., Debgupta, J., Pillai, V. K. & Shelke, M. V. C@SiNW/TiO₂ core-shell nanoarrays with sandwiched carbon passivation layer as high efficiency photoelectrode for water splitting. *Sci. Rep.* <https://doi.org/10.1038/srep04897> (2014).
47. Liu, C., Yang, Y., Li, J. & Chen, S. Phase transformation synthesis of TiO₂/CdS heterojunction film with high visible-light photoelectrochemical activity. *Nanotechnology* <https://doi.org/10.1088/1361-6528/aabd6e> (2018).

Acknowledgements

The authors would like to thankfully acknowledge the Institute for Nanotechnology and Water Sustainability of the University of South Africa and the National Research Foundation, South Africa (Grant number: 112066 and 130743) for financially supporting this work.

Author contributions

William Moloto: Conceptualization, Formal analysis, Investigation, Methodology, Writing—review and editing
Pontsho Mbule: Formal analysis, Investigation, Methodology, Writing—review and editing. Edward Nxumalo: Formal analysis, Investigation, Methodology, Writing—review and editing. Bulelwa Ntsendwana: Conceptualization, Formal analysis, Investigation, Methodology, Writing—review and editing.

Competing interests

The authors declare no competing interests.

Additional information

Supplementary Information The online version contains supplementary material available at <https://doi.org/10.1038/s41598-024-61701-3>.

Correspondence and requests for materials should be addressed to E.N. or B.N.

Reprints and permissions information is available at www.nature.com/reprints.

Publisher's note Springer Nature remains neutral with regard to jurisdictional claims in published maps and institutional affiliations.



Open Access This article is licensed under a Creative Commons Attribution 4.0 International License, which permits use, sharing, adaptation, distribution and reproduction in any medium or format, as long as you give appropriate credit to the original author(s) and the source, provide a link to the Creative Commons licence, and indicate if changes were made. The images or other third party material in this article are included in the article's Creative Commons licence, unless indicated otherwise in a credit line to the material. If material is not included in the article's Creative Commons licence and your intended use is not permitted by statutory regulation or exceeds the permitted use, you will need to obtain permission directly from the copyright holder. To view a copy of this licence, visit <http://creativecommons.org/licenses/by/4.0/>.

© The Author(s) 2024